

Original Article

# Wildebeest Habit Optimizer with Deep Learning-Based Histopathological Image Analysis for Breast Cancer Diagnosis

R. Gurumoorthy<sup>1</sup>, M. Kamarasan<sup>2</sup>

<sup>1,2</sup>Department of Computer and Information Science, Annamalai University, Annamalainagar, India.

<sup>1</sup>Corresponding Author : saragopi76@gmail.com

Received: 01 April 2023

Revised: 07 June 2023

Accepted: 21 June 2023

Published: 21 July 2023

**Abstract** - Automatic categorization of Breast Cancer (BC) Histopathological Image (HPI) is a major research study in the biomedical informatics domain because of the great medical eminence of classification in offering prognosis and diagnosis of BC. Computer-Aided Diagnosis (CAD) of BC histopathologic images is a significant tool to improve the efficiency and precision of BC classification and diagnosis. Machine Learning (ML) models are trained on large sets of HPI images to detect features and patterns linked with different stages and types of BC. This could aid pathologists in making more precise detections and developing potential treatment plans. Therefore, this study develops a Wildebeest Habit Optimizer with Deep Learning based Histopathological Image Analysis for Breast Cancer Diagnosis (WHODL-HIABCD) technique. The presented WHODL-HIABCD technique exploits Bilateral Filtering (BF) based noise removal process to get rid of the noise. Followed by the WHODL-HIABCD technique uses an EfficientNet model with a WHO-based hyperparameter optimizer for feature extraction purposes. Finally, the Attention-based Bidirectional Gated Recurrent Unit (ABiGRU) method was utilized for classifying and recognizing BC. The investigational results of the WHODL-HIABCD technique are experimented with the benchmark dataset. The comparative study stated the enhanced performance of the WHODL-HIABCD technique than recent models.

**Keywords** - Breast cancer, Hyperparameter tuning, Histopathological images, Computer-Aided Diagnosis, Deep learning.

## 1. Introduction

BC ranks first as the most common female cancer across the world. Moreover, the BC mortality rate is extremely high than other cancer [1]. The histopathological analysis is the broadly utilized approach for BC diagnosis despite current advancements in understanding the molecular biology of BC evolution and finding relevant molecular markers [2]. In the face of significant growth achieved by diagnostic imaging technologies, the final BC detection, which includes staging and grading, is done by implementing a visual assessment of histological samples under the microscopes [3]. Digital pathology is a technology that allows the digitalization of tissue samples into digital images and attempts to mimic the pathologist by presenting computing methods for examination. To identify fine data and details that cannot be easily identified by the naked eye, computational techniques in digital pathology were utilized [4]. Even though the advent of these new technologies, precise treatment and diagnosis remains a challenge. The assortment of treatment processes for BC mainly hinges on the precise classification of tumor from Histopathological Images (HPI), but lacking experienced and skilful pathologists, along with the over-

tiredness of the pathologist, rarely might cause misclassification that undoubtedly leads to misdiagnosis [5].

Manual assessment techniques present three types of error, which includes distributional, statistical, and human errors in low-magnification images [6]. Such issues adversely affect the precision of the differential classification in classical cancer detection. Hence, a reproducible and automated technique could handle the aforementioned problems potentially [24].

CAD established approaches for robust valuation of medical image-related examination. A promising strategy is presented for facilitating tumour staging and grading while avoiding unnecessary expenditures [8]. Orthodox ML and image-processing approaches necessitate wide pre-processing, segmentation and manual abstraction of particular visual features before classification [9]. But DL methods have exceeded human achievement in visual tasks by applying automatic ranking classification and feature extraction by multi-layers to be implemented for detecting cancer with the tumor tissue slides [10].



This study develops a Wildebeest Habit Optimizer with Deep Learning based Histopathological Image Analysis for Breast Cancer Diagnosis (WHODL-HIABCD) technique. The presented WHODL-HIABCD technique exploits Bilateral Filtering (BF) based noise removal process to get rid of the noise. Followed by the WHODL-HIABCD technique uses an EfficientNet model with a WHO-based hyperparameter optimizer for feature extraction purposes. Finally, the Attention-based Bidirectional Gated Recurrent Unit (ABiGRU) method is utilized for classifying and recognizing BC. The investigational results of the WHODL-HIABCD technique are experimented with the benchmark dataset.

## 2. Related Works

In [11], introduced a Residual Dual-Shuffle Attention Network (DRDA-Net), dual-shuffling attention-assisted DL method. Motivated by the bottleneck units of the ShuffleNet structure, in this presented technique, a channel attention system has been incorporated by the author that improvised the ability of the method to study the intricate image forms. Further, the densely connected blocks of the method addressed the vanishing gradient problem and overfitting, though the method was well-trained on small data. In [12], a patch-associated DL termed Pa-DBN-BC was modelled to recognize and categorize BC on histopathologic images assisted with DBN. With un- and supervised pre-trained and fine-tuned segments, features were put under extraction. From image patches, the network automatically extracts attributes. LR is utilized to categorize the patches from HPI images.

Chattopadhyay et al. [13] presented a Multi-Scale Dual Residual Recurrent Network (MTRRE-Net), a new end-to-end DL approach for BC categorization from HIS imageries. This study presents a conflicting technique of dual residual block integrated with RNN for resolving the gradient vanishing issue. Liu et al. [14] propose a Multi-Scale Multi-View Progressive Feature Encoding Network (MSMV-PFENet) model for classifying effectively. In relation to the cell nuclei density, the author has chosen the regions pertaining to carcinogenesis at several scaling from a discrete view. A bidirectional LSTM examined the encrypting vectors to acquire category scores, and lastly, the majority voting approach combined diverse views to categorize the histopathological images.

In [15], rather than depending on a single CNN approach, a new rank-based ensemble approach was devised by merging outcomes of 3 TL-CNN methods called MobileNetV3\_Small, GoogleNet, and VGG11. The presented ensemble method was modelled through the Gamma function to sort out a 2-class classifier problem of breast HIS images. Man et al. [16] present a new technique called DenseNet121-AnoGAN to categorize breast HIS images into benevolent and malevolent classes. This

presented method has 2 major parts: utilizing DenseNet to abstract multi-layer factors of the discriminatory patching and utilizing an unsupervised Anomaly Detection with GAN (AnoGAN) for screening mislabelled patches.

## 3. The Proposed Model

In this research, an innovative WHODL-HIABCD approach for automatic identification and categorization of BC is presented. The presented WHODL-HIABCD approach comprises BF-based noise elimination, EfficientNet feature extraction, WHO tuning process, and ABiGRU-based categorization. Fig. 1 represents the comprehensive flow of the WHODL-HIABCD method.

### 3.1. Image Pre-processing

In the initial phase, the BF technique is used to get rid of the noise in the input images. It can be referred to as a nonlinear image filtering approach that can be utilized to smooth images at the same time preserving details and edges [25]. It is beneficial to remove noises from images along with those sharpening and enhancing edges. It operates by calculating pixel robustness' weighted average in the total surrounding pixels, where the spatial distancing and the intensity variance among pixels decide the weights. This indicates that pixels with similar locations and intensities were given more weight in the averaging procedure, whereas pixels with distinct locations or intensities were given less weight.

### 3.2. Feature Extraction

At this stage, the WHODL-HIABCD technique uses the EfficientNet model for feature extraction. The main ideology of the EfficientNet is to utilize a compound scaling technique that balances the network's resolution, depth, and width at all stages of the structures [18]. The technique scales the network in a principled manner by raising the network resolution, depth, and width concurrently. This EfficientNet structure has the support of stacked convolution layers, then a completely associated classification layer, and global average-pool layering. The convolution layers utilize an integration of regular convolutions and depthwise separable convolutions for minimalizing the computing cost and parameters.

EfficientNet techniques can be labelled by a scaling variable determining the network resolution, depth, and width. The EfficientNet-B0 has few FLOPs and parameters, while the EfficientNet-B7 is the largest method and has additional FLOPs and parameters. It was pre-trained on large image data like ImageNet and has attained existing performance on several CV tasks like segmentation, image classification, and object detection. It is broadly utilized in TL applications, whereas the pre-trained EfficientNet approach is fine-tuned on the small dataset for the particular task. Fig. 2 highlights the structure of the EfficientNet method.

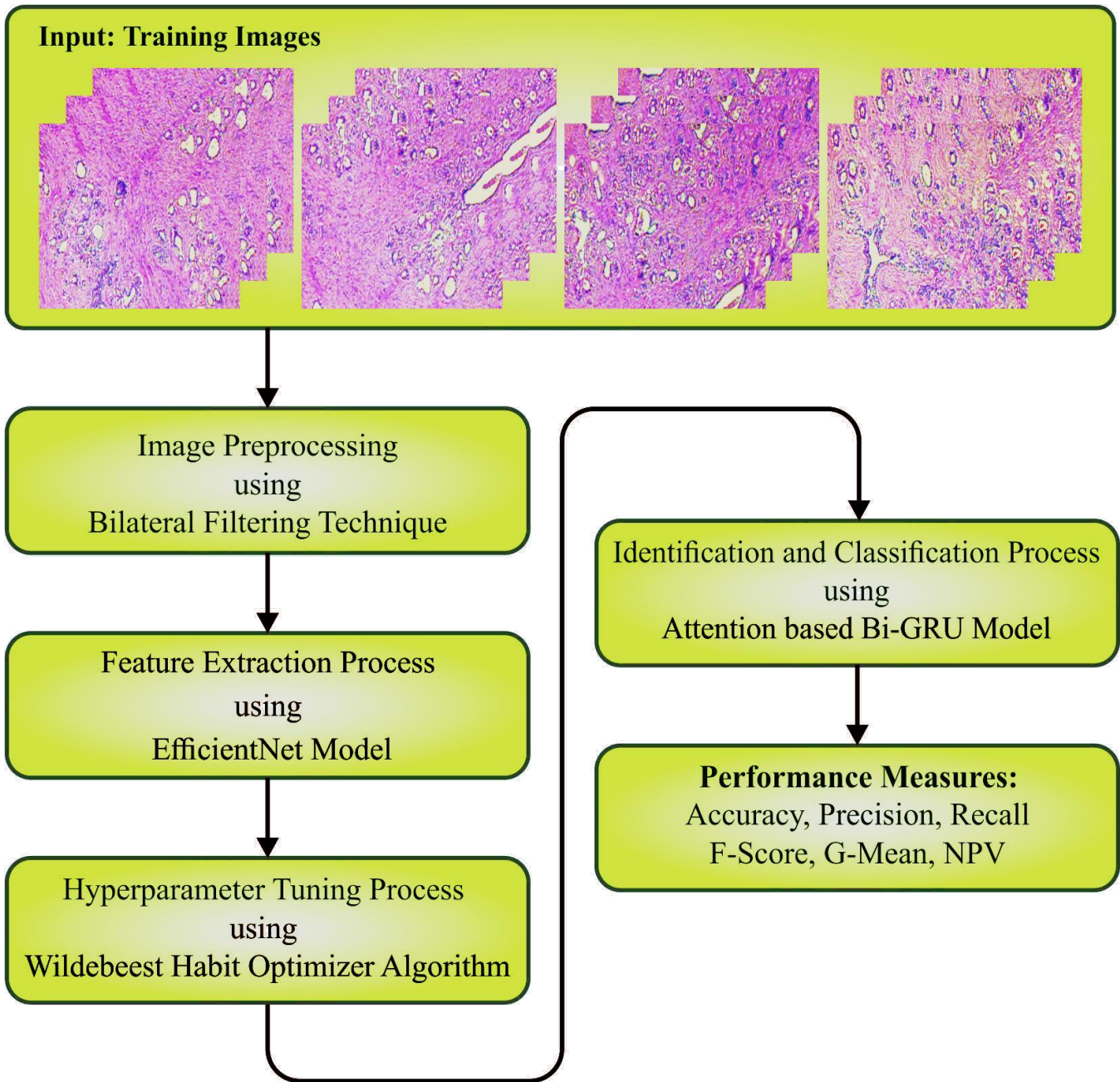


Fig. 1 Overall flow of WHODL-HIABCD approach

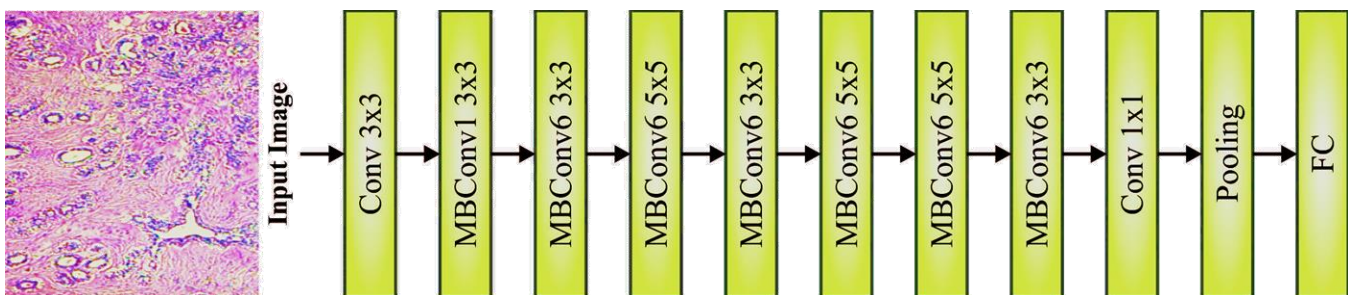


Fig. 2 Structure of EfficientNet model

For hyperparameter tuning, the WHO algorithm is used to adjust the hyperparameters of the WHO algorithm. Wildebeests' food-searching practice serves as the method for the WHO technique [19]. Wildebeest is an active, sociable mammal that finds food sources. To attract females for mating, males compete in sex challenges with rivals. The population (wildebeest) was initialized randomly as a candidate at the beginning of the WHO approach. The population was constrained between lower ( $X_{\min}$ ) and upper ( $X_{\max}$ ) limitations

$$X_i \in [X_{\min}, X_{\max}] \quad (1)$$

Where,  $I = 1, 2, \dots, N$ .

Subsequently, the wildebeest applied the milling technique of displacement. Continues to find the optimum location while taking the constant ( $n$ ) as a scarce randomization displacement. The competitor in position  $X$  had employed a random stage  $Z_n$  that should regularly find the ( $n$ ) spots. Therefore, the localized experimental stage  $Z_n$  was generated by the subsequent equation:

$$Z_n = X_i + \varepsilon \times \theta \times v \quad (2)$$

In Eq. (2),  $v$  denotes the random unit vector,  $\theta'$  denotes the random integer within  $[0, 1]$ ;  $X_i$  denotes the  $i$ -th candidate number, and  $\varepsilon$  denotes the learning rate.

Afterwards, estimating a constant ( $n$ ) of trivial random possibility, the wildebeest attuned its position to attain the best random location.

$$X_i = \alpha_1 \times Z_n^* + \beta_1 \times (X_i - Z_n^*) \quad (3)$$

In Eq. (3),  $\alpha_1$  and  $\beta_1$  leader variables denote the candidate's local displacement. Modelling the swarm behavior of wildebeest was the last step. It can be imitated afterwards, assigning the rest of the competitors to a spot with proper food sources,

$$X_i = \alpha_2 \times X_i + \beta_2 \times X_h \quad (4)$$

In Eq. (4),  $X_h$  signifies a random candidate and  $\alpha_2$  and  $\beta_2$  denotes the leader variable to direct the local movement of the crew.

$$X_i = X_i + \theta \times (x_{\max} - X_{\min}) \times \bar{v} \quad (5)$$

In Eq. (5),  $V$  denotes the random unit vector.

There was a population once the grassland had massive productivity. This model is named individual pressure. It is utilized for completing the task, and the optimal contender utilizes Eq. (6) to destroy other contenders.

$$if(\|X^* - X_i\| < \eta, (\|X^* - X_i\| > 1) \quad (6)$$

$$Then X_i = X^* + \varepsilon \times \hat{n} \quad (7)$$

Here,  $\eta$  signifies a threshold to avoid location crowding, and  $\hat{n}$  specifies the amount of reachable segments neighboring the best solution.

In the last stage, the social remembrance of the swarm was put under simulation to provide better placements and was defined as follows:

$$X = X^* + 0.1 \times \bar{v} \quad (8)$$

Lastly, the optimum value was initialized to the hyperparameter of the classifier. The optimized value gives  $1 \times 10^{-6}$ : rate of weight decay, 0.001: rate of learning, 8: the size of the batch, 40%: dropout rate with L2 regulation, and 0.8: momentum.

The WHO algorithm has derived a fitness function to have better categorizer achievement. It determined a positive value for representing the ideal achievement of the candidate solutions. Here, the reduced error rate of the classifier is the fitness function, as specified in Eq. (9).

$$\begin{aligned} fitness(x_i) &= ClassifierErrorRate(x_i) \\ &= \frac{number\ of\ misclassified\ samples}{Total\ number\ of\ samples} * 100 \end{aligned} \quad (9)$$

### 3.3. Image Classification

To classify the images for BC detection, the ABiGRU model is used. Despite outstanding RNN performance for non-linear time series prediction, it generally suffers from exploding or vanishing gradient problems, mainly confined to its capacity to implement time series prediction [20] accurately. Thus, a modified version of RNN, such as the BiGRU model, is proposed to classify BC. Remarkably, the BiGRU model is easy to converge and requires comparatively less parameters compared with LSTM that drastically decreasing the overfitting risk. This method considers the fusion of two GRU models in which one moves forward to study the time sequence pattern, and the other moves in the contrary direction to describe the time sequence. These assurances that this technique learns backwards and forward non-linear dependency.

Especially the GRU has a Reset ( $R$ ) and an Update ( $Z$ ) gate, where the  $R$  controls the amount of data forgotten at time  $t - 1$ , and the  $Z$  controls the prominence of the hidden layer of the past moment at  $t$  time. Moreover,  $Z$  can be used for learning the long-term, whereas  $R$  can be used for learning the short-term dependencies. Firstly, consider the input sequence.  $X_t$ , the computation mechanism of the backwards-moving GRU ( $\overleftarrow{GRU}$ ) and the forward-moving GRU ( $\overrightarrow{GRU}$ ) is expressed as follows: correspondingly.

$$\begin{cases} \vec{Z}_t = \sigma(\vec{X}_t \cdot \vec{W}_{XZ} + \vec{H}_{t-1} \cdot \vec{W}_{HZ} + \vec{b}_Z) \\ \vec{R}_t = \sigma(\vec{X}_t \cdot \vec{W}_{XR} + \vec{H}_{t-1} \cdot \vec{W}_{HR} + \vec{b}_R) \\ \vec{H}'_t = \sigma(\vec{X}_t \cdot \vec{W}_{XH'} + \vec{R}_t \cdot \vec{H}_{t-1} \cdot \vec{W}_{H'H'} + \vec{b}_H) \\ \vec{H}_t = \vec{Z}_t \odot \vec{H}_{t-1} + (1 - \vec{Z}_t) \odot \vec{H}'_t \end{cases} \quad (10)$$

$$\begin{cases} \vec{Z}_t = \sigma(\vec{X}_t \cdot \vec{W}_{XZ} + \vec{H}_{t-1} \cdot \vec{W}_{HZ} + \vec{b}_Z) \\ \vec{R}_t = \sigma(\vec{X}_t \cdot \vec{W}_{XR} + \vec{H}_{t-1} \cdot \vec{W}_{HR} + \vec{b}_R) \\ \vec{H}'_t = \sigma(\vec{X}_t \cdot \vec{W}_{XH'} + \vec{R}_t \cdot \vec{H}_{t-1} \cdot \vec{W}_{H'H'} + \vec{b}_H) \\ \vec{H}_t = \vec{Z}_t \odot \vec{H}_{t-1} + (1 - \vec{Z}_t) \odot \vec{H}'_t \end{cases} \quad (11)$$

Where  $b$  shows the bias term.  $\odot$  represent the component-wise multiplication,  $H_t$  and  $H'_t$  represents Hidden State ( $H$ ) and candidate  $H$  during time  $t$ , correspondingly;  $\sigma(\cdot)$  denotes the activation function; and  $W_{XZ}, W_{HZ}, W_{XR}, W_{HR}, W_{XH'}, W_{H'H'}$  symbolize the weight matrix to be learned.

Furthermore, the  $\vec{H}_t$  and  $\vec{H}'_t$  are combined to attain the last representation of  $H_f$   $H$ , as shown below.

$$H_t = \vec{H}_t \oplus \vec{H}'_t \quad (12)$$

Eq. (12)  $\oplus$  indicates the component-wise addition. Finally, the output of RNN ( $O_t$ ) is expressed as follows:

$$O_t = \sigma(W_O \cdot H_t + b_y) \quad (13)$$

As a variant of the attention module, the Self-Attention Mechanism (SAM) reduces dependency on exterior data and is proficient in characterizing the interior relation of input factors. As compared with other DL techniques, the SAM identify the main characteristics of the input feature instead of treating each feature equally and providing their respective weight to describe their importance. Hence, the SAM helps increase computational efficacy and is conducive to enhancing model generalization. Targeting improving the generalization and input feature's interpretability, the SAM was intended to measure and identify the prominence of output and input features. It specifically focuses on the significant feature in the hidden layer that strengthens its generalization and improves the computation efficacy. Then, the computation model of the SAM introduced the steps.

**Step 1:** Evaluate the attention score (bias term). Assume the input series  $x^k = (x_1^k, x_2^k, \dots, x_n^k)$ , we attain the bias term  $error_t^m$  at  $t$  time and  $m$  dimension, as follows.

$$error_t^m = f(W_{t,m}[H_{1,m}, H_{2,m}, \dots, H_{T,M}] + U_{t,m}x^k) \quad (14)$$

In Eq. (14),  $f(\cdot)$  indicates the dense layer;  $M$  and  $T$  denote the  $H$  dimension and time step amount;  $t = \{1, \dots, T\}$  and  $m = \{1, \dots, M\}$ ;  $W$  and  $U$  show weight matrix that should be fitted.

**Step 2:** Calculate feature importance (attention weight) of  $m$ -th feature at  $t$  time by implementing the *softmax* function, as follows.

$$\omega_t^m = \frac{\exp(error_t^m)}{\sum_{k=1}^T \exp(error_t^m)}, \sum_t \omega_t^m = 1 \quad (15)$$

**Step 3:** According to the average value of feature reconstruction  $\omega_t^{\overline{mean}}$  given in Eq. (16), the newest  $H$  ( $H_t^{\text{attention}}$ ) at  $t$  time is attained, as follows:

$$\omega_t^{\overline{mean}} = \frac{1}{M} \sum_{m=1}^M \omega_t^m \quad (16)$$

$$H_t^{\text{attention}} = \omega_t^{\overline{mean}} H_t \quad (17)$$

## 4. Results and Discussion

In this research, the investigational outputs of the WHODL-HIABCD model are tested on the BreakHIS dataset [21]. The dataset contains two subsets, namely 40X and 100X datasets, as given in Table 1. The dataset includes benign and malignant classes. Fig. 3 represents the sample benign and malignant images.

Four histological types of benign BC: Tubular Adenoma (TA), Adenosis (A), Phyllodes Tumor (PT), and Fibroadenoma (F), and four Malignant Carcinomas (BC): Mucinous (MC), Ductal (DC), Papillary (PC), and Lobular (LC).

The confusion matrix of the WHODL-HIABCD method is illustrated in Fig. 4. The figure indicates that the WHODL-HIABCD technique recognized the benign and malignant samples.

In Table 2 and Fig. 5, the grades of the WHODL-HIABCD algorithm are portrayed on the 40X dataset. The experimental values defined that the WHODL-HIABCD technique effectually recognizes benign and malignant instances. As a sample, on 70% of TRP, the WHODL-HIABCD method gains average  $accu_{bal}$  of 91.56%,  $prec_n$  of 94.36%,  $reca_l$  of 91.56%,  $spec_y$  of 91.56%,  $F_{score}$  of 92.56%, and MCC of 85.88%. In parallel, on 30% of TSP, the WHODL-HIABCD method acquires average  $accu_{bal}$  of 92.12%,  $prec_n$  of 92.87%,  $reca_l$  of 92.12%,  $spec_y$  of 92.12%,  $F_{score}$  of 92.48%, and MCC of 84.98%.

Table 1. Details on databases

Class	Magnification	
	40X	100X
Benign	652	644
Malignant	1370	1437
<b>Overall</b>	<b>1995</b>	<b>2081</b>

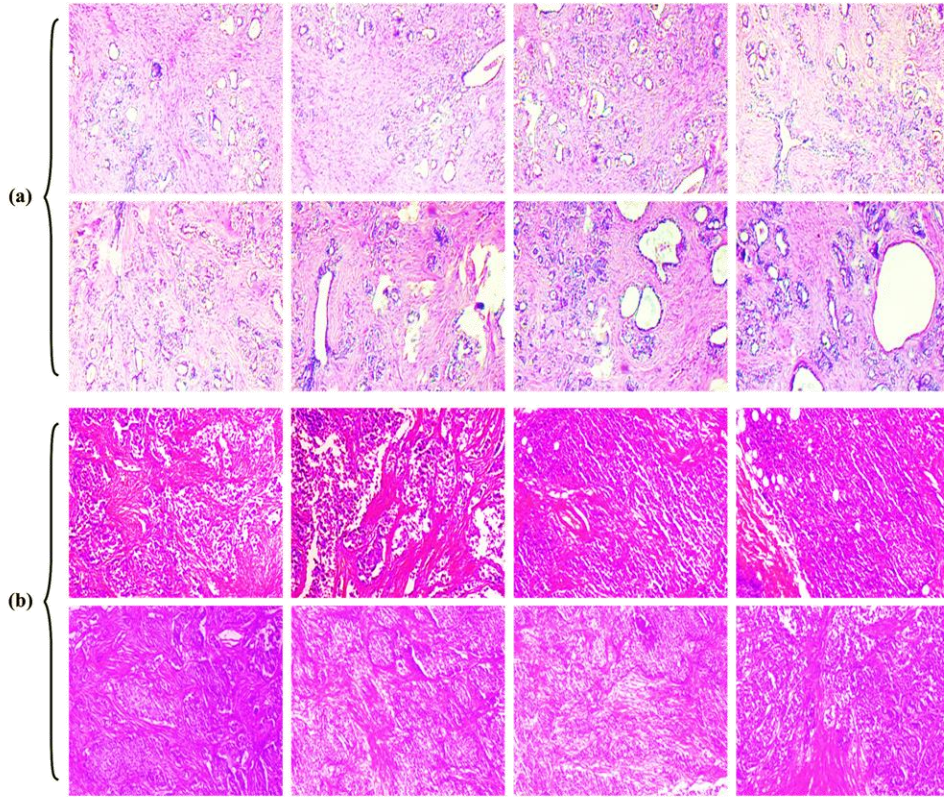


Fig. 3 a) Benign images b) Malignant images

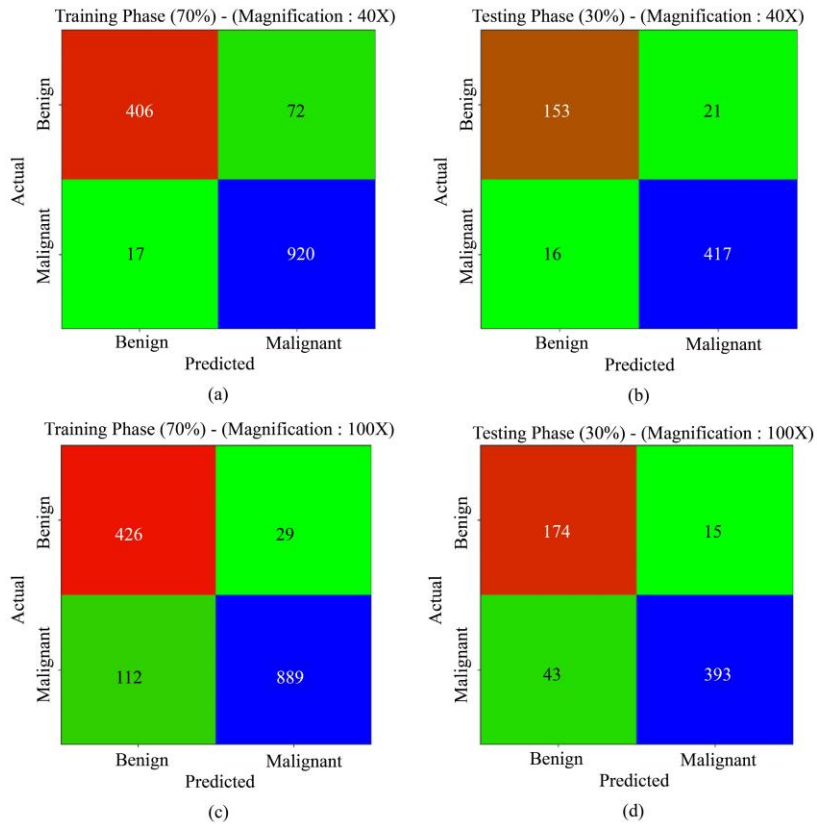
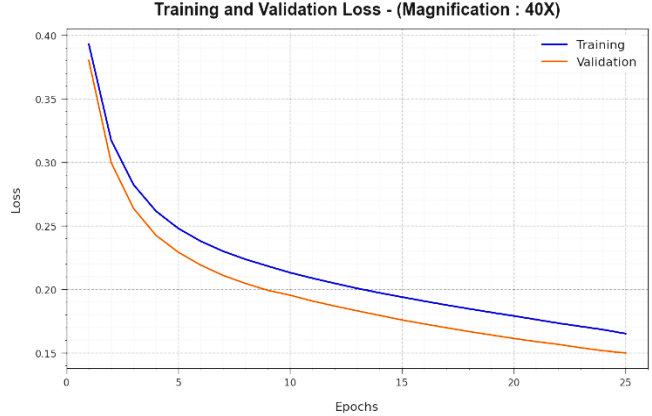


Fig. 4 Confusion matrices of (a-b) and (c-d) 70% and 30% of TRP/TSP on 40X and 100X dataset

**Table 2. Classifier output of WHODL-HIABCD model on 40X dataset**

Magnification: 40X						
Class	$Accu_{bal}$	$Prec_n$	$Reca_l$	$Spec_y$	$F_{score}$	MCC
Training Phase (70%)						
Benign	84.94	95.98	84.94	98.19	90.12	85.88
Malignant	98.19	92.74	98.19	84.94	95.39	85.88
<b>Average</b>	<b>91.56</b>	<b>94.36</b>	<b>91.56</b>	<b>91.56</b>	<b>92.75</b>	<b>85.88</b>
Testing Phase (30%)						
Benign	87.93	90.53	87.93	96.30	89.21	84.98
Malignant	96.30	95.21	96.30	87.93	95.75	84.98
<b>Average</b>	<b>92.12</b>	<b>92.87</b>	<b>92.12</b>	<b>92.12</b>	<b>92.48</b>	<b>84.98</b>



**Fig. 7 Loss curve of WHODL-HIABCD technique on 40X dataset**

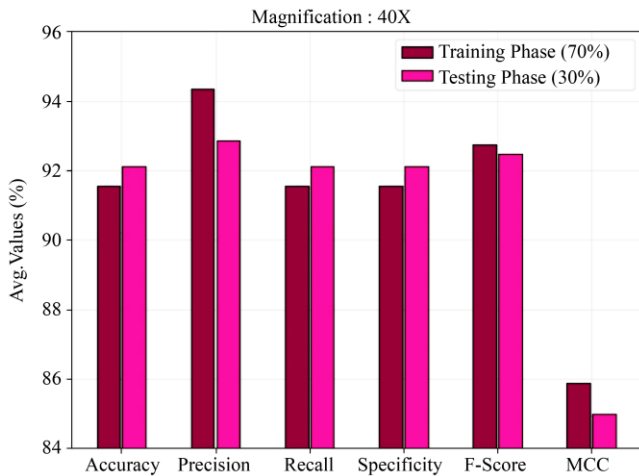


**Fig. 5 Average output of WHODL-HIABCD model on 40X dataset**

Fig. 6 inspects the accuracy of the WHODL-HIABCD approach at the time of the T&V process on the 40X dataset. The figure notified that the WHODL-HIABCD approach reached a greater accuracy value over growing epochs. Also, the growing validation accuracy over training illustrates that the WHODL-HIABCD technique learns effectively on a 40X dataset.

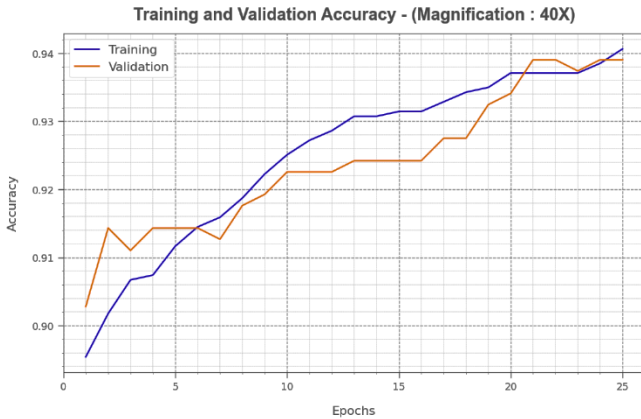


**Fig. 6 Accuracy curve of WHODL-HIABCD method on 40X dataset**

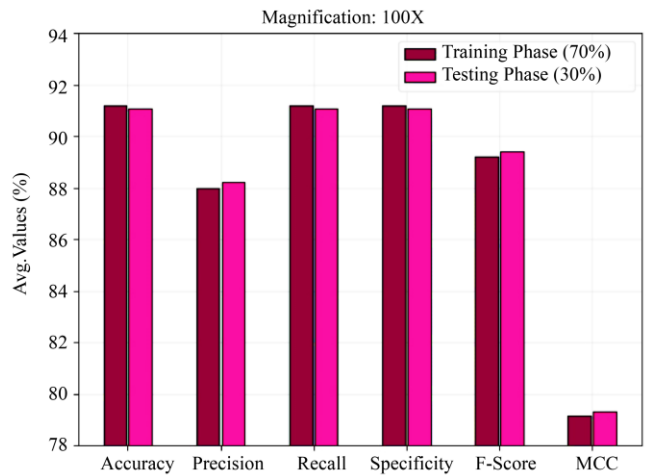


**Fig. 8 Average output of WHODL-HIABCD technique on 100X dataset**

The loss evaluation of the WHODL-HIABCD method during Training and Validation (T&V) is given on the 40X dataset in Fig. 7. The figure specifies that the WHODL-HIABCD methodology attains closer training values and validation loss values. The WHODL-HIABCD methodology learns effectively on a 40X dataset.

In Table 3 and Fig. 8, the outputs of the WHODL-HIABCD approach are depicted on the 100X dataset. The figure depicted that the WHODL-HIABCD methodology recognizes benign and malignant samples effectually.

As a sample, on 70% of TRP, the WHODL-HIABCD methodology acquires average  $accu_{bal}$  of 91.22%,  $prec_n$  of 88.01%,  $reca_l$  of 91.22%,  $spec_y$  of 91.22%,  $F_{score}$  of 89.23%, and MCC of 79.17%.

In parallel, on 30% of TSP, the WHODL-HIABCD method acquires average  $accu_{bal}$  of 91.10%,  $prec_n$  of 88.25%,  $reca_l$  of 91.10%,  $spec_y$  of 91.10%,  $F_{score}$  of 89.42%, and MCC of 79.30%.

Table 3. Classifier output of WHODL-HIABCD technique on 100X dataset

Magnification: 100X						
Class	$Accu_{bal}$	$Prec_n$	$Reca_l$	$Spec_y$	$F_{score}$	MCC
Training Phase (70%)						
Benign	93.63	79.18	93.63	88.81	85.80	79.17
Malignant	88.81	96.84	88.81	93.63	92.65	79.17
<b>Average</b>	<b>91.22</b>	<b>88.01</b>	<b>91.22</b>	<b>91.22</b>	<b>89.23</b>	<b>79.17</b>
Testing Phase (30%)						
Benign	92.06	80.18	92.06	90.14	85.71	79.30
Malignant	90.14	96.32	90.14	92.06	93.13	79.30
<b>Average</b>	<b>91.10</b>	<b>88.25</b>	<b>91.10</b>	<b>91.10</b>	<b>89.42</b>	<b>79.30</b>

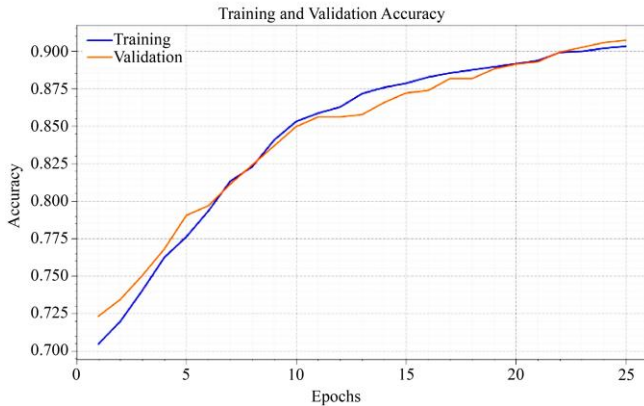


Fig. 9 Accuracy curve of WHODL-HIABCD technique on 100X dataset

Fig. 9 inspects the WHODL-HIABCD method’s accuracy during the T&V process on the 100X dataset. The figure notified that this model achieved a growing accuracy value over growing epochs. Moreover, the growing validation accuracy over training shows that the WHODL-HIABCD model learned effectively on the 100X dataset.

The loss analysis of the WHODL-HIABCD methodology during T&V is given on the 100X dataset in Fig. 10. The figure specifies that the WHODL-HIABCD methodology attains closer T&V loss values. The WHODL-HIABCD approach learns effectively on the 100X dataset.

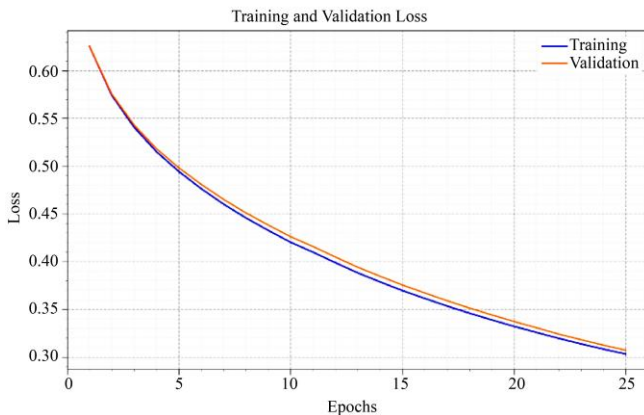


Fig. 10 Loss curve of WHODL-HIABCD methodology on 100X dataset

Table 4. Relative output of WHODL-HIABCD model with other techniques on 40X dataset

Magnification: 40X				
Techniques	$Accu_y$	$Prec_n$	$Reca_l$	$F_{score}$
WHODL-HIABCD	92.12	92.87	92.12	92.48
PFTAS-QDA	84.08	83.98	83.61	83.81
Inception-V3	73.66	79.9	82.04	81.58
ResNet50	79.42	77.01	88.09	86.18
Inception-ResNetV2	77.53	81.3	87.34	84.01
Xception	80.18	79.81	85.35	86.27

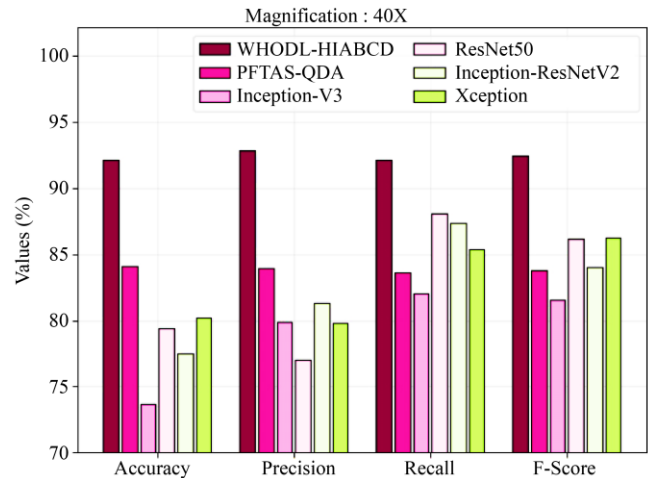


Fig. 11 Relative analysis of WHODL-HIABCD model on 40X dataset

Table 4 and Fig. 11, the comparative outputs of the WHODL-HIABCD approach are provided on the 40X dataset.

Based on  $accu_y$ , the WHODL-HIABCD technique offers to increase  $accu_y$  of 92.12% while the PFTAS-QDA, Inception-v3, ResNet50, Inception-ResNetv2, and Xception algorithms reach decreasing  $accu_y$  of 84.08%, 73.66%, 79.42%, 77.53%, and 80.18% respectively. In the meantime, based on  $prec_n$ , the WHODL-HIABCD approach offers to increase  $prec_n$  of 92.87% while the PFTAS-QDA, Inception-v3, ResNet50, Inception-ResNetv2, and Xception techniques attain decreasing  $prec_n$  of 83.98%, 79.9%, 77.01%, 81.3%, and 79.81% correspondingly. Eventually, based on  $reca_l$ , the WHODL-HIABCD method offers increasing  $reca_l$  of 92.12% while the PFTAS-QDA, Inception-v3, ResNet50, Inception-ResNetv2, and Xception techniques reach decreasing  $reca_l$  of 83.61%, 82.04%, 88.09%, 87.34%, and 85.35% correspondingly.

In Fig. 12, a ROC examination of the WHODL-HIABCD methodology is exhibited on the 40X dataset. The figure depicted that the WHODL-HIABCD methodology gave an output to the enhanced value of ROC. Also, it is evident that the WHODL-HIABCD algorithm can outspread the improved value of ROC on the total classes.

**Table 5. Comparative outcome of WHODL-HIABCD method with other methods on 100X dataset**

Magnification: 100X				
Methods	$Accu_y$	$Prec_n$	$Recal_l$	$F_{score}$
WHODL-HIABCD	91.22	88.01	91.22	89.23
PFTAS-QDA	82.64	82.64	82.51	81.58
Inception-V3	76.96	92.03	69.25	80.51
ResNet50	71.26	72.97	88.12	81.57
Inception-ResNetV2	70.45	91.31	63.14	74.45
Xception	81.85	89.07	84.87	86.91

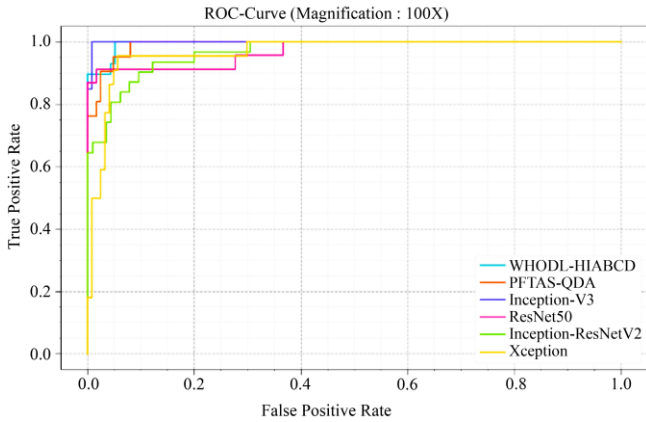


**Fig. 12 ROC curve of WHODL-HIABCD approach on 40X dataset**

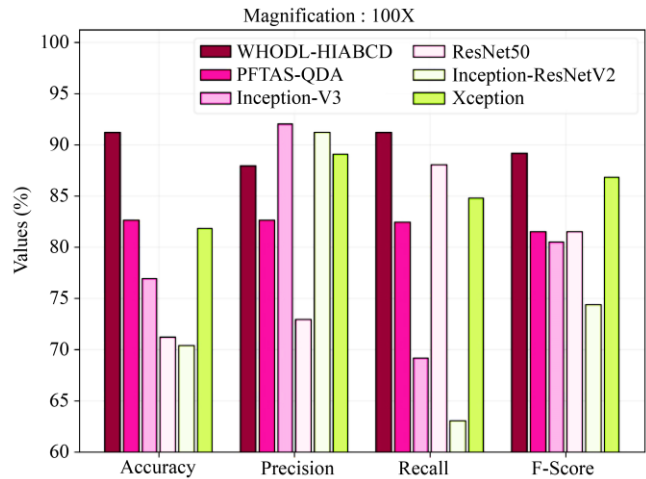


**Fig. 13 Comparative analysis of WHODL-HIABCD approach on 100X dataset**

Table 5 and Fig. 13, the comparative outputs of the WHODL-HIABCD method are provided on the 100X dataset [22]. Based on  $accu_y$ , the WHODL-HIABCD technique offers increasing  $accu_y$  of 91.22% while the PFTAS-QDA, Inception-v3, ResNet50, Inception-ResNetv2, and Xception models obtain decreasing  $accu_y$  of 82.64%, 76.96%, 71.26%, 70.45%, and 81.85% respectively.

**References**

[1] S. Alkassar et al., “Going Deeper: Magnification-Invariant Approach for Breast Cancer Classification using Histopathological Images,” *IET Computer Vision*, vol. 15, no. 2, pp. 151-164, 2021. [CrossRef] [Google Scholar] [Publisher Link]

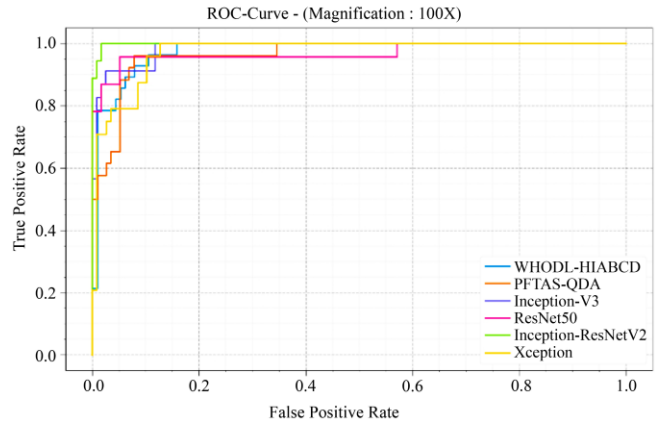


**Fig. 14 ROC curve of WHODL-HIABCD approach on 100X dataset**

Meanwhile, based on  $prec_n$ , the WHODL-HIABCD algorithm offers increasing  $prec_n$  of 88.01% while the PFTAS-QDA, Inception-v3, ResNet50, Inception-ResNetv2, and Xception methods acquire decreasing  $prec_n$  of 82.64%, 92.03%, 72.97%, 91.31%, and 89.07% correspondingly.

Finally, based on  $recal_l$ , the WHODL-HIABCD method offers increasing  $recal_l$  of 91.22% while the PFTAS-QDA, Inception-v3, ResNet50, Inception-ResNetv2, and Xception techniques reach decreasing  $recal_l$  of 82.51%, 69.25%, 88.12%, 63.14%, and 84.87% respectively. These outputs assured the improved categorization outputs of the WHODL-HIABCD model.

In Fig. 14, a ROC examination of the WHODL-HIABCD algorithm is exhibited on the 100X dataset. The figure labeled that the WHODL-HIABCD algorithm leads to an enhanced value of ROC. However, the WHODL-HIABCD method can outspread an improved value of ROC on each class label.

**5. Conclusion**

In this work, a novel WHODL-HIABCD technique for automatic identification and categorization of BC. The presented WHODL-HIABCD technique comprises BF-based noise elimination, EfficientNet feature extraction, WHO hyperparameter tuning, and ABiGRU-based classification.

The application of the WHO technique assists in the optimal hyperparameter selection of the ABiGRU method, which helps in accomplishing an improved detection rate. The experimental outcomes of the WHODL-HIABCD method are tested with the benchmark dataset. The comparative study stated the enhanced performance of the WHODL-HIABCD technique to recent approaches.

- [2] Yiping Zhou, Can Zhang, and Shaoshuai Gao, "Breast Cancer Classification from Histopathological Images Using Resolution Adaptive Network," *IEEE Access*, vol. 10, pp. 35977-35991, 2022. [[CrossRef](#)] [[Google Scholar](#)] [[Publisher Link](#)]
- [3] Md Zahangir Alom et al., "Breast Cancer Classification from Histopathological Images with Inception Recurrent Residual Convolutional Neural Network," *Journal of Digital Imaging*, vol. 32, no. 4, pp. 605-617, 2019. [[CrossRef](#)] [[Google Scholar](#)] [[Publisher Link](#)]
- [4] Mahesh Gour, Sweta Jain, and T. Sunil Kumar, "Residual Learning Based CNN for Breast Cancer Histopathological Image Classification," *International Journal of Imaging Systems and Technology*, vol. 30, no. 3, pp. 621-635, 2020. [[CrossRef](#)] [[Google Scholar](#)] [[Publisher Link](#)]
- [5] Ebrahim Mohammed Senan et al., "Classification of Histopathological Images for Early Detection of Breast Cancer Using Deep Learning," *Journal of Applied Science and Engineering*, vol. 24, no. 3, pp. 323-329, 2021. [[CrossRef](#)] [[Google Scholar](#)] [[Publisher Link](#)]
- [6] Rania R. Kadhim, and Mohammed Y. Kamil, "Evaluation of Machine Learning Models for Breast Cancer Diagnosis via Histogram of Oriented Gradients Method and Histopathology Images," *International Journal on Recent and Innovation Trends in Computing and Communication*, vol. 10, no. 4, pp. 36-42, 2022. [[CrossRef](#)] [[Google Scholar](#)] [[Publisher Link](#)]
- [7] G. Rajasekaran, and C. Sunitha Ram, "Effective Breast Cancer Prediction Based on Feature Extraction, Fusion and Selection using Hybrid Methodologies," *SSRG International Journal of Electrical and Electronics Engineering*, vol. 10, no. 5, pp. 131-142, 2023. [[CrossRef](#)] [[Publisher Link](#)]
- [8] K. Sabeena Beevi, Madhu S. Nair, and G.R Bindu, "Automatic Mitosis Detection in Breast Histopathology Images using Convolutional Neural Network Based Deep Transfer Learning," *Biocybernetics and Biomedical Engineering*, vol. 39, no. 1, pp. 214-223, 2019. [[CrossRef](#)] [[Google Scholar](#)] [[Publisher Link](#)]
- [9] B. Devanathan, and M. Kamarasan, "Multi-Objective Archimedes Optimization Algorithm with Fusion-Based Deep Learning Model for Brain Tumor Diagnosis and Classification," *Multimedia Tools and Applications*, vol. 82, pp. 16985-17007, 2023. [[CrossRef](#)] [[Google Scholar](#)] [[Publisher Link](#)]
- [10] Tahir Mahmood et al., "Artificial Intelligence-Based Mitosis Detection in Breast Cancer Histopathology Images using Faster R-CNN and Deep CNNs," *Journal of Clinical Medicine*, vol. 9, no. 3, p. 749, 2020. [[CrossRef](#)] [[Google Scholar](#)] [[Publisher Link](#)]
- [11] Soham Chattopadhyay et al., "DRDA-Net: Dense Residual Dual-Shuffle Attention Network for Breast Cancer Classification Using Histopathological Images," *Computers in Biology and Medicine*, vol. 145, 2022. [[CrossRef](#)] [[Google Scholar](#)] [[Publisher Link](#)]
- [12] Irum Hirra et al., "Breast Cancer Classification from Histopathological Images using Patch-Based Deep Learning Modeling," *IEEE Access*, vol. 9, pp. 24273-24287, 2021. [[CrossRef](#)] [[Google Scholar](#)] [[Publisher Link](#)]
- [13] Soham Chattopadhyay et al., "MTRRE-Net: A Deep Learning Model for Detection of Breast Cancer from Histopathological Images," *Computers in Biology and Medicine*, vol. 150, 2022. [[CrossRef](#)] [[Google Scholar](#)] [[Publisher Link](#)]
- [14] Linxian Liu et al., "Classification of Breast Cancer Histology Images Using MSMV-PFENet," *Scientific Reports*, vol. 12, no. 1, 2022. [[CrossRef](#)] [[Google Scholar](#)] [[Publisher Link](#)]
- [15] Samridha Majumdar, Payel Pramanik, and Ram Sarkar, "Gamma Function based Ensemble of CNN Models for Breast Cancer Detection in Histopathology Images," *Expert Systems with Applications*, vol. 213, 2023. [[CrossRef](#)] [[Google Scholar](#)] [[Publisher Link](#)]
- [16] Rui Man, Ping Yang, and Bowen Xu, "Classification of Breast Cancer Histopathological Images using Discriminative Patches Screened by Generative Adversarial Networks," *IEEE Access*, vol. 8, pp. 155362-155377, 2020. [[CrossRef](#)] [[Google Scholar](#)] [[Publisher Link](#)]
- [17] V. Shalini, and K. S. Angel Viji, "Integration of Convolutional Features and Residual Neural Network for the Detection and Classification of Leukemia from Blood Smear Images," *International Journal of Engineering Trends and Technology*, vol. 70, no. 9, pp. 176-184, 2022. [[CrossRef](#)] [[Publisher Link](#)]
- [18] Ayat Abedalla et al., "Chest X-Ray Pneumothorax Segmentation using U-Net with Efficientnet and Resnet Architectures," *PeerJ Computer Science*, vol. 7, 2021. [[CrossRef](#)] [[Google Scholar](#)] [[Publisher Link](#)]
- [19] Sai Sambasiva Rao Bairaboina, and Srinivasa Rao Battula, "Ghost-ResNeXt: An Effective Deep Learning Based on Mature and Immature WBC Classification," *Applied Sciences*, vol. 13, no. 6, p. 4054, 2023. [[CrossRef](#)] [[Google Scholar](#)] [[Publisher Link](#)]
- [20] Tong Niu et al., "A Hybrid Deep Learning Framework Integrating Feature Selection and Transfer Learning for Multi-Step Global Horizontal Irradiation Forecasting," *Applied Energy*, vol. 326, 2022. [[CrossRef](#)] [[Google Scholar](#)] [[Publisher Link](#)]
- [21] [Online]. Available: <https://web.inf.ufpr.br/vri/databases/breast-cancer-histopathological-database-breakhis/>
- [22] Min Liu et al., "Breast Histopathological Image Classification Method Based on Autoencoder and Siamese Framework," *Information*, vol. 13, no. 3, p. 107, 2022. [[CrossRef](#)] [[Google Scholar](#)] [[Publisher Link](#)]
- [23] Anish Anurag et al., "Local Attention-Based Descriptor Definition using Vision Transformer for Breast Cancer Identification," *International Journal of Engineering Trends and Technology*, vol. 70, no. 12, pp. 317-327, 2022. [[CrossRef](#)] [[Publisher Link](#)]

- [24] Nouman Ahmad, Sohail Asghar, and Saira Andleeb Gillani, "Transfer Learning-Assisted Multi-Resolution Breast Cancer Histopathological Images Classification," *The Visual Computer*, vol. 38, no. 8, pp. 2751-2770, 2022. [[CrossRef](#)] [[Google Scholar](#)] [[Publisher Link](#)]
- [25] Caixia Liu, and Mingyong Pang, "One-Dimensional Image Surface Blur Algorithm based on Wavelet Transform and Bilateral Filtering," *Multimedia Tools and Applications*, vol. 80, no. 19, pp. 28697-28711, 2021. [[CrossRef](#)] [[Google Scholar](#)] [[Publisher Link](#)]